REPORT

MAGNETISM

Chirally coupled nanomagnets

Zhaochu Luo[1,2]*, Trong Phuong Dao[1,2,3], Aleš Hrabec[1,2,3], Jaianth Vijayakumar[2], Armin Kleibert[2], Manuel Baumgartner[3], Eugenie Kirk[1,2], Jizhai Cui[1,2], Tatiana Savchenko[2], Gunasheel Krishnaswamy[3], Laura J. Heyderman[1,2]*, Pietro Gambardella[3]*

Magnetically coupled nanomagnets have multiple applications in nonvolatile memories, logic gates, and sensors. The most effective couplings have been found to occur between the magnetic layers in a vertical stack. We achieved strong coupling of laterally adjacent nanomagnets using the interfacial Dzyaloshinskii-Moriya interaction. This coupling is mediated by chiral domain walls between out-of-plane and in-plane magnetic regions and dominates the behavior of nanomagnets below a critical size. We used this concept to realize lateral exchange bias, field-free current-induced switching between multistate magnetic configurations as well as synthetic antiferromagnets, skyrmions, and artificial spin ices covering a broad range of length scales and topologies. Our work provides a platform to design arrays of correlated nanomagnets and to achieve all-electric control of planar logic gates and memory devices.

Engineering the coupling between magnetic elements is central to fundamental advances in magnetism and spintronics. The discovery of interlayer coupling between two ferromagnetic layers separated by a nonmagnetic spacer, caused by the Ruderman-Kittel-Kasuya-Yosida interaction, has led to the realization of synthetic antiferromagnets (*1*–*3*) and the discovery of giant magnetoresistance (*4*, *5*). Similarly, the exchange bias between ferromagnetic and antiferromagnetic layers (*6*) is widely used to stabilize the magnetic reference layer in spin valves and magnetic tunnel junctions (*7*, *8*). These couplings are highly effective in vertically stacked structures. However, in order to realize two-dimensional (2D) networks of nanoscale magnetic elements, it is desirable to engineer effective lateral couplings in a controllable way. So far, this has been achieved by exploiting long-range dipolar interactions (*9*–*12*). However, the dipolar interaction is nonlocal and scales inversely with the volume of the magnets, which limits its use in applications that involve nanometer-sized structures and thin films.

Here, we demonstrate an alternative mechanism with which to control the lateral coupling between adjacent magnetic nanostructures. Our concept is based on the interfacial Dzyaloshinskii-Moriya interaction (DMI), $H_{DM} = -\boldsymbol{D}_{ij} \cdot (\boldsymbol{m}_i \times \boldsymbol{m}_j)$, which embodies the antisymmetric exchange coupling between two neighboring magnetic moments $\boldsymbol{m}_i$ and $\boldsymbol{m}_j$ induced by the spin-orbit interaction in a structurally asymmetric environment (*13*, *14*). In contrast to the symmetric exchange interaction, which favors a parallel alignment of the magnetic moments, the DMI favors an orthogonal orientation of $\boldsymbol{m}_i$ relative to $\boldsymbol{m}_j$, with a fixed chirality given by the direction of the Dzyaloshinskii-vector $\boldsymbol{D}_{ij}$. At the interface between a magnetic layer and a heavy metal, the DMI can be strong enough to induce the formation of noncollinear spin textures such as spin spirals (*15*) and skyrmions (*16*, *17*). Often, however, the competition between the DMI, the exchange interaction, and the magnetic anisotropy in thin films with out-of-plane (OOP) magnetization results in the formation of chiral domain walls separating large regions with uniform up or down magnetic moments (*18*, *19*). In these systems, the DMI also plays a crucial role in determining the direction and speed of current-induced domain wall motion (*20*–*23*). We exploited the DMI to control the lateral coupling between OOP and in-plane (IP) magnetic structures (Fig. 1A) and demonstrate distinct phenomena associated with such chirally coupled nanomagnets.

We fabricated arrays of nanomagnets that combine strong DMI with regions exhibiting IP and OOP magnetic anisotropy. The arrays were fabricated from Pt (6 nm)/Co (1.6 nm)/AlO_x trilayers patterned by means of electron beam lithography and Ar ion milling (*24*). Here, AlO_x refers to an Al layer that is oxidized in an oxygen plasma. Such magnetic trilayers have a large DMI (*25*, *26*) as well as tunable magnetic anisotropy, which is IP or OOP depending on

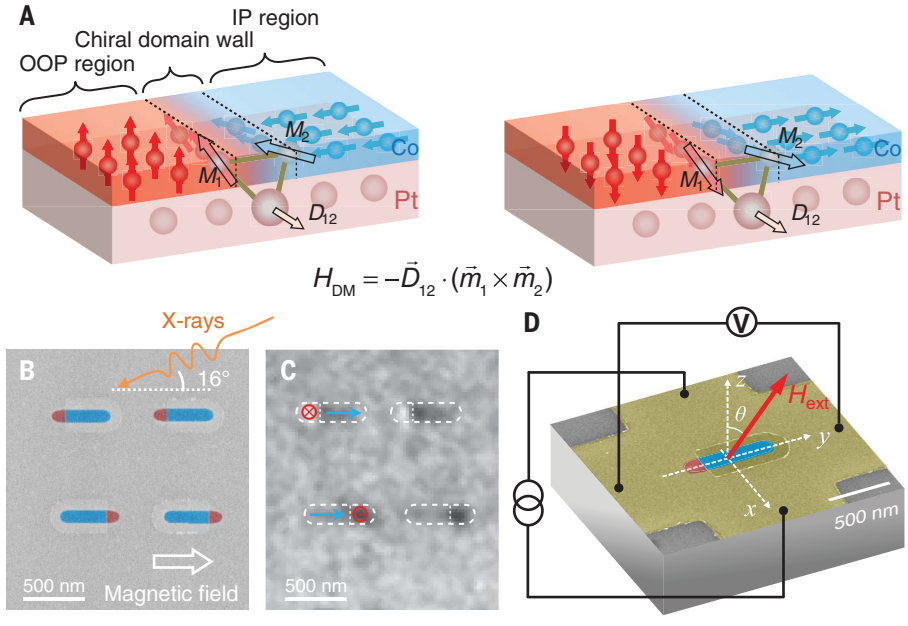

Fig. 1. Chiral coupling between OOP and IP magnets. (**A**) Schematics of the coupled magnetization states favored by the DMI in adjacent OOP and IP regions of a Pt/Co/AlO_x trilayer. (**B**) Scanning electron micrograph of coupled OOP-IP elements fabricated by means of electron-beam lithography. Red and blue colors indicate regions with OOP and IP magnetization, respectively. (**C**) X-PEEM image with bright and dark magnetic contrast in the OOP regions corresponding to ↓ and ↑ magnetization, respectively. The dark gray contrast in the IP regions corresponds to → magnetization, determined by taking images at different sample orientations with respect to the x-ray direction (*24*). The direction of the incident x-rays and the IP magnetic field used for prealignment are indicated with arrows. (**D**) Schematic of an OOP-IP element fabricated on top of a Hall cross for electrical measurements.

[1]Laboratory for Mesoscopic Systems, Department of Materials, ETH Zurich, 8093 Zurich, Switzerland. [2]Paul Scherrer Institut, 5232 Villigen PSI, Switzerland. [3]Laboratory for Magnetism and Interface Physics, Department of Materials, ETH Zurich, 8093 Zurich, Switzerland.
***Corresponding author. Email: zhaochu.luo@psi.ch (Z.L.); laura.heyderman@psi.ch (L.J.H.); pietro.gambardella@mat.ethz.ch (P.G.).**

the degree of oxidation of the Co/Al interface (fig. S1) (*27*), and are widely used as a model system for the study of current-induced switching and domain wall motion in spintronic devices (*28*, *29*). A scanning electron micrograph of an array of Co elements, each consisting of adjacent IP and OOP regions, is shown in Fig. 1B. The size and shape of the IP magnetized region is controlled by covering the Al with a thin Ta protective layer to prevent oxidation during the oxygen plasma process.

X-ray photoemission electron microscopy (X-PEEM) images provide first evidence that the magnetizations of the OOP and IP regions are coupled and that this coupling is chiral. If the magnetization of the IP region points to the right ("→"), after saturation with an IP magnetic field, OOP regions on the left and right of the IP region point down ("↓") and up ("↑"), respectively (Fig. 1C). The relative orientation between OOP and IP parts is thus either ↓→ or →↑, which agrees with the left-handed chirality expected from the negative sign of the DMI in Pt/Co/AlO_x (*25*). As expected, reversing the direction of the IP field leads to the observation of ↑← and ←↓ coupling (fig. S8).

To further analyze the chiral coupling between OOP and IP regions, we measured the anomalous Hall resistance of OOP-IP Co/AlO_x elements fabricated on top of a Pt Hall cross (Fig. 1D) as a function of external magnetic field. Because the anomalous Hall effect is proportional to the *z*-component of the magnetization, these measurements reflect the state of the OOP region, with the IP magnetization preset by an IP field applied parallel to *y*. For an external field $H_{ext}//z$, we found that the hysteresis loop of the OOP region shifts by more than 200 Oe toward positive or negative fields for right or left orientation of the IP magnetization, respectively (Fig. 2A). These opposite shifts indicate that the DMI strongly favors the ↓→ and ↑← configurations, resulting in an effective exchange bias field H_{bias}, whose sign can be tuned by presetting the orientation of the IP magnetization. Hence, the chiral coupling demonstrated here provides a method with which to realize large hysteresis bias in lateral structures.

When the external field is applied IP, $H_{ext}//y$, we additionally find that the OOP region switches direction simultaneously with the IP region (Fig. 2, B and C, and fig. S3). Starting from the DMI-stable ↑← configuration, the OOP region switches from up to down as the IP field switches the IP magnetization from ← to →, thus avoiding the unfavorable ↑→ configuration. This observation implies that the energy associated with the chiral coupling is larger than the energy of the barrier to switch the OOP region, so that the direction of the IP magnetization effectively controls the OOP magnetization. If the applied magnetic field is tilted in the *y*-*z* plane, the field can also induce the switching of the OOP region, which then biases the IP magnetization. Therefore, depending on the coercivity of the OOP and IP regions and on the tilt angle θ of the external field, we observed switching between different multistate magnetic configurations (Fig. 2B). If both the OOP and IP field components of the applied magnetic field assisted the DMI-favored configurations, we observed bistable switching between the ↓→ and ↑← states (type I behavior, similar to $H_{ext}//y$). By contrast, if the two field components preferred the DMI-unfavored ↓← and ↑→ configurations, we observed switching between all the four possible combinations of states, with the sequence determined by the relative amplitude of the IP and OOP magnetic field components (type II and type III behavior).

The switching of the OOP-IP elements can be modeled with two coupled OOP and IP macrospins (*24*), where the energy of each configuration ($E_{↑→}$, $E_{↓→}$, $E_{↑←}$, and $E_{↓←}$) is given by the sum of the Zeeman energy and the energy

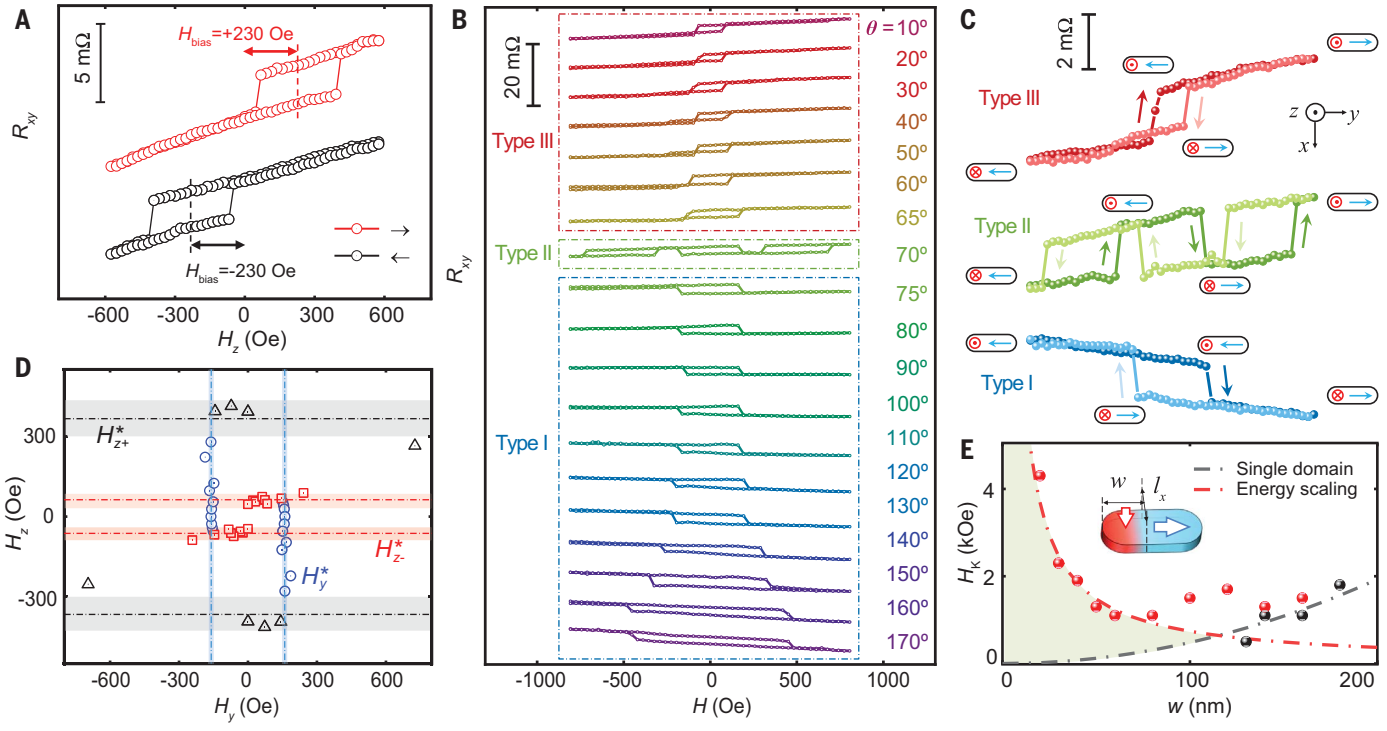

Fig. 2. Exchange bias and field-induced switching of chirally coupled OOP-IP elements. (**A**) OOP magnetization as a function of H_z for the OOP-IP element shown in Fig. 1D for the magnetization in the IP region pointing → and ←. The hysteretic jumps of the anomalous Hall resistance R_{xy} indicate switching of the OOP magnetization. The linear increase of R_{xy} with field is caused by the gradual tilt of the IP magnetization toward the *z* axis. (**B**) Magnetic hysteresis loops for a magnetic field tilted in the *y*-*z* plane for various tilt angles θ. (**C**) Multistate switching configurations III, II, and I corresponding to the hysteresis loops for θ = 30°, 70°, and 140° shown in (B). (**D**) Critical switching field H^*_{z+} (black triangles), H^*_{z-} (red squares), and H^*_y (blue circles) of the OOP region. The lines are fits according to the macrospin model described in the text, with errors indicated by the shaded regions. (**E**) Boundaries of the single-domain behavior (black line) and chiral-coupling (red line) as a function of the OOP magnetic anisotropy field H_K and element size *w*. The red and black points are determined from micromagnetic simulations. The shaded area indicates the range of parameters for which chiral coupling determines the magnetic configuration.

associated with the DMI between the magnetic moments of the OOP and IP regions, $\boldsymbol{M}_{OOP}$ and $\boldsymbol{M}_{IP}$: $E = -(\boldsymbol{M}_{OOP} + \boldsymbol{M}_{IP}) \cdot \boldsymbol{H}_{ext} - \boldsymbol{D} \cdot (\boldsymbol{M}_{OOP} \times \boldsymbol{M}_{IP})$. Assuming that the OOP and IP magnetization switch whenever the energy difference between two configurations is larger than the energy barrier for magnetization reversal ΔE_{OOP} and ΔE_{IP}, respectively, the critical switching fields for the OOP and IP regions are given by $H^*_{z\pm} = (\Delta E_{OOP} \pm E_{DM})/2M_{OOP}$ and $H^*_y = (\Delta E_{IP} + E_{DM})/2M_{IP}$, respectively, where E_{DM} is the chiral coupling energy. As expected from the model, the switching fields of the OOP region determined experimentally lie on horizontal and vertical lines of an H_z-H_y diagram (Fig. 2D). We therefore identify these lines as the critical fields $H^*_{z\pm}$ and H^*_y. From these data, we determined the value of E_{DM} = 3.5 ± 0.3 eV and the DMI constant D = −0.9 ± 0.1 mJ/m^2, which is in good agreement with previous estimates of the DMI in Pt/Co/AlO$_x$ (*25*).

Because E_{DM} is proportional to the length l_x of the quasi-1D domain wall separating the OOP and IP regions, whereas ΔE_{OOP} is proportional to the area $l_x w$, where w is the width of the OOP region (Fig. 2E, inset), the ratio $E_{DM}/\Delta E_{OOP} \propto 1/w$ increases when decreasing the dimensions of the

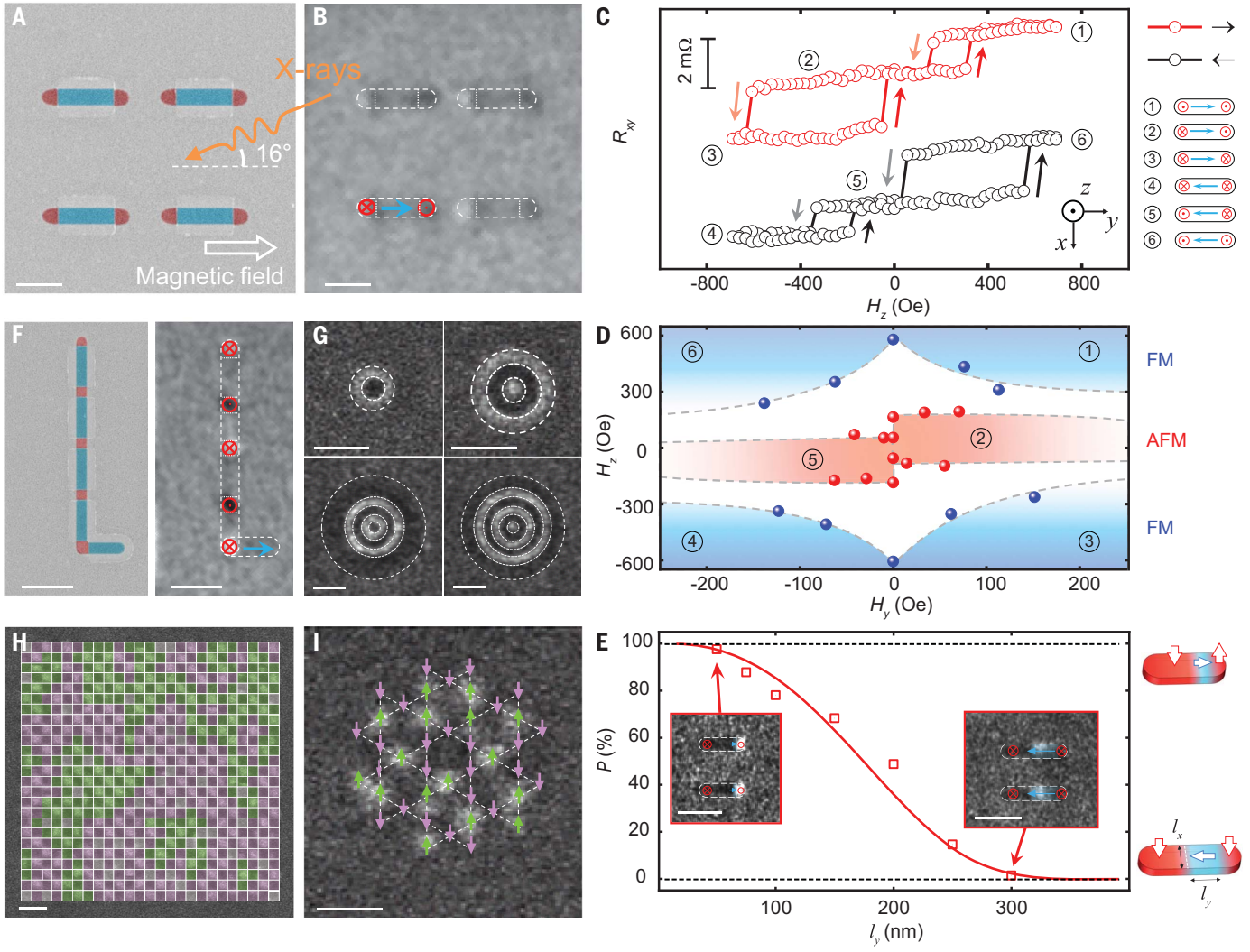

Fig. 3. Lateral synthetic antiferromagnets based on chiral coupling. (**A**) Scanning electron micrograph of coupled OOP-IP-OOP elements and (**B**) corresponding X-PEEM image. The stable magnetic configuration of the OOP-IP-OOP element is ↓ → ↑ after prealignment of the IP region with an IP field pointing →. (**C**) Magnetic hysteresis of an OOP-IP-OOP element as a function of H_z for two opposite orientations of the IP spacer. The six possible magnetic configurations are shown. (**D**) H_z versus H_y phase diagram of the OOP-IP-OOP element used for (C). The red and blue dots are the critical fields delimiting the antiferromagnetic and ferromagnetic alignments, respectively, of the two OOP regions. In the white shaded area, the configuration depends on the history of the magnetization. (**E**) Probability of correlated switching resulting in antiferromagnetically aligned OOP regions as a function of the length l_y of the IP spacer. Saturating fields are applied, first $-H_y$ and then $-H_z$, before applying a field H_z and measuring the magnetic state of the element. Each data point is averaged over 41 different elements. (Insets) MFM images of OOP-IP-OOP elements with l_y = 50 and 300 nm. The bright and dark MFM contrast corresponds to ↑ and ↓ magnetizations, respectively. (**F**) Scanning electron micrograph and X-PEEM image of a chain structure including five OOP regions, which align antiparallel after a field has been applied perpendicular to the chain (parallel to the lowest IP region). (**G**) MFM images of synthetic skyrmions with one, two, four, and five IP rings after saturation with a magnetic field $-H_z$. (**H**) MFM image of an artificial spin system consisting of OOP elements on a square lattice acting as Ising-like moments coupled by means of IP spacers after saturating with a magnetic field $-H_z$. Antiferromagnetic domains are shaded in green and purple. (**I**) MFM image of an artificial kagome spin system after saturating with a magnetic field $-H_z$. The green and purple arrows indicate the orientation of the magnetization of the OOP vertices. All X-PEEM and MFM images have been recorded at zero field. Scale bars, 500 nm.

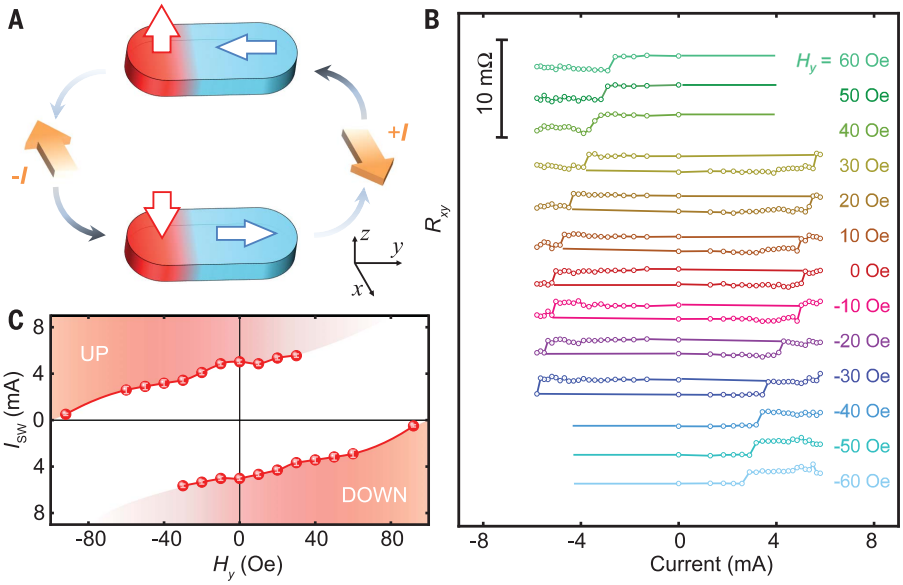

Fig. 4. Field-free current-induced magnetization switching of OOP-IP elements. (**A**) Schematic of the current-induced switching of an OOP-IP element. The device geometry is shown in Fig. 1D; the area of the OOP region is about 120 by 120 nm. (**B**) Magnetization loops as a function of applied current for different values of H_y. The measurements are performed by injecting 50-μs-long current pulses and measuring the anomalous Hall resistance R_{xy} after each pulse. Changes in R_{xy} indicate switching of the OOP region. The switching at zero field is symmetric with respect to the current, whereas $H_y > 0$ helps to switch the OOP region ↓ and decrease the negative switching current, and $H_y < 0$ helps to switch the OOP region ↑ and decrease the positive switching current. (**C**) Critical switching current I_{SW} as a function of H_y. The range of parameters leading to deterministic switching between ↑ and ↓ states is shaded in red.

element. Hence, below a critical size, the magnetic behavior of the OOP region is predominantly determined by the chiral coupling. The boundaries that delimit this region are defined by $E_{DM}/\Delta E_{OOP} > 1$ and the single-domain condition $w < w_{SD} \propto \sqrt{H_K}$, where w_{SD} and H_K are the critical single-domain dimension and the OOP effective anisotropy field, respectively. These boundaries are shown in Fig. 2E together with the results of micromagnetic simulations that provide additional support to our model (fig. S10) (*24*). A similar reasoning can be applied to model the influence of the OOP magnetization on the IP magnetization, taking into account that the IP anisotropy is shape-dependent. The favorable scaling of $E_{DM}/\Delta E_{OOP}$ and $E_{DM}/\Delta E_{IP}$ toward reduced dimensions means that chiral coupling can be exploited to control the magnetization of small systems. In our case, the thermal stability factor is $E_{DM}/k_BT \approx 140$ at room temperature, where k_B is the Boltzmann constant and T is the temperature, so the width w of the patterned element can be reduced down to 35 nm while retaining a thermal stability larger than 40 k_BT.

We now illustrate possible applications of chiral coupling. First, we discuss the fabrication of tailor-made laterally coupled synthetic antiferromagnetic structures, skyrmions, and artificial spin systems. As a starting point, we considered two separate OOP regions that are coupled by an IP spacer. X-PEEM imaging revealed that the static orientation of two OOP elements connected by an IP spacer is antiparallel and that, if the IP magnetization is preset with a magnetic field to the right, the OOP-IP-OOP magnetization is ↓→↑ (Fig. 3, A and B), which is in agreement with the left-handed chirality imposed by the DMI. The behavior of these structures was characterized by their anomalous Hall resistance in an applied field (Fig. 3C). To differentiate the two OOP regions, one side was made smaller than the other. For $H_{ext}//z$, the flat curve between the two shifted hysteresis loops in Fig. 3C indicates that the OOP regions are coupled antiparallel at low field, whereas the parallel orientation can only be enforced by magnetic fields larger than 400 to 600 Oe. The ↑↓ and ↓↑ antiferromagnetic states at zero magnetic field were set by prealigning the IP magnetization to be ← or →, respectively. The antiferromagnetic state at zero field was achieved independently of the initial orientation and amplitude of the field. Similar to the OOP-IP element, all the possible combinations of states 1 to 6 shown in Fig. 3C can be reached by changing the direction of the field in the *y*-*z* plane (Fig. 3D).

As long as the IP spacer retains a monodomain state, the two OOP elements effectively interact with each other. Thus, reversing the magnetization of one OOP element with a field $H_{ext}//z$ causes the reversal of the IP spacer and subsequently the reversal of the other OOP element. In addition, magnetic force microscopy (MFM) measurements (Fig. 3E) demonstrate that the effective antiferromagnetic coupling between the OOP elements is a function of the IP spacer length l_y, leading to correlated reversal events for $l_y < 300$ nm and a nearly 100% correlated switching probability for $l_y \leq 50$ nm. These measurements were performed on structures that include two OOP elements with different sizes, so that the largest element switches with, and the smallest element switches against, the external field H_z. OOP-IP-OOP structures with $l_y > 1$ μm (fig. S11A) and curvilinear geometries (fig. S11C) also have alternate up- and down-magnetized OOP regions. However, in such cases, the IP regions might assume a multidomain configuration and can effectively be replaced with two separate IP connectors. These two short sections can then be used to control the OOP magnetization in a nonlocal way. For all these structures, we found that the effective antiferromagnetic interaction mediated by chiral coupling is orders of magnitude stronger than the dipolar coupling between magnets of the same size and separation (fig. S6).

Coupled OOP and IP elements can be further used as building blocks of more complex spin systems that have a well-defined symmetry and topology. In Fig. 3F, a linear chain that consists of five OOP and IP regions is shown with alternating OOP magnetic moments. Such a structure can be used to propagate magnetic information from one end of the chain to the other. Synthetic Néel skyrmions can also be realized by coupling concentric OOP rings with 50-nm-wide circular IP spacers (Fig. 3G). By patterning more IP rings, we can create skyrmionic structures that do not have a counterpart in unpatterned thin films, with a topological charge that alternates between ±1 and 0 (so-called skyrmioniums or target skyrmions) depending on the number of rings. Such structures might be of interest to study high-frequency excitations of skyrmions as well as for the generation and transmission of spin waves in magnonic crystals. Last, strongly coupled artificial spin systems, with Ising-like OOP elements connected by IP elements, can be created. Examples with the OOP elements arranged on a square and a kagome lattice are given in Fig. 3, H and I, respectively. The correlated Ising-like moments lead to the spontaneous formation of domains with antiferromagnetic ordering for the square lattice and frustrated behavior for the kagome lattice with highly degenerate low energy states.

Another interesting application concerns the current-induced switching of magnetic elements, which is a basic requirement for the all-electrical operation of integrated nonvolatile magnetic memory and logic devices. Our measurements show that the OOP and IP regions can be simultaneously switched by an electric current flowing in the Pt/Co layer, orthogonal to the IP magnetization (Fig. 4). The switching is caused by the current-induced spin-orbit torques that originate from the spin Hall and interface effects found in ferromagnets adjacent to heavy metal layers

(*28*–*31*). Such electrical switching cannot be implemented in dipolar-coupled magnetic elements, which are usually too thick to be manipulated by spin torques. Moreover, the chiral coupling enables entirely field-free switching of the OOP magnetization, which is difficult to achieve in isolated OOP elements (*32*–*36*). In Fig. 4B, we show that the OOP region switches deterministically in zero field for a current I_{SW} = 5 mA injected parallel to x. Applying a field $H_{ext}//\pm y$ along the IP easy axis leads to a decrease or increase of the switching current, which is proportional to H_{ext} (Fig. 4C). We interpret this behavior as the field assisting or counteracting the reversal of the IP magnetization that is driven by the damping-like component of the spin-orbit torque. This suggests that the current drives the switching of the IP magnetization (*30*, *37*) and that the reversal of the OOP region is a consequence of the chiral coupling. Because the current density that is required to switch the IP magnetization is typically lower than that required by the OOP magnetization (fig. S5C) (*37*, *38*), OOP-IP coupled structures offer an efficient and scalable approach to field-free switching of magnetic devices, which is furthermore compatible with the materials and processes currently used in the fabrication of magnetic memories.

The coupled OOP-IP building blocks demonstrated here can be used to fabricate synthetic antiferromagnets with linear and curved geometries, synthetic skyrmions, and artificial spin ices. Indeed, the spontaneous formation of the ground state after magnetization in an athermal artificial spin ice network reflects the strong nearest-neighbor interactions in these systems, which is likely to lead to interesting frustrated behavior. Furthermore, the multiplicity of magnetic states that can be stabilized in OOP-IP elements combined with all-electric synchronous switching opens a route for the realization of nanomagnet logic gates and memory devices as well as for the design of electrically reconfigurable magnonic crystals, which can be used to manipulate the propagation of spin waves in synthetic media or provide a controlled modulation of the magnetic stray field in hybrid materials, such as ferromagnet/semiconductor and ferromagnet/superconductor heterostructures.

REFERENCES AND NOTES

1. P. Grünberg, R. Schreiber, Y. Pang, M. B. Brodsky, H. Sowers, *Phys. Rev. Lett.* **57**, 2442–2445 (1986).
2. S. S. Parkin, N. More, K. P. Roche, *Phys. Rev. Lett.* **64**, 2304–2307 (1990).
3. R. A. Duine, K. J. Lee, S. S. P. Parkin, M. D. Stiles, *Nat. Phys.* **14**, 217–219 (2018).
4. M. N. Baibich *et al*., *Phys. Rev. Lett.* **61**, 2472–2475 (1988).
5. G. Binasch, P. Grünberg, F. Saurenbach, W. Zinn, *Phys. Rev. B Condens. Matter* **39**, 4828–4830 (1989).
6. J. Nogués, I. K. Schuller, *J. Magn. Magn. Mater.* **192**, 203–232 (1999).
7. B. Dieny *et al*., *Phys. Rev. B Condens. Matter* **43**, 1297–1300 (1991).
8. S. S. Parkin *et al*., *J. Appl. Phys.* **85**, 5828–5833 (1999).
9. R. P. Cowburn, M. E. Welland, *Science* **287**, 1466–1468 (2000).
10. A. Imre *et al*., *Science* **311**, 205–208 (2006).
11. R. F. Wang *et al*., *Nature* **439**, 303–306 (2006).
12. L. J. Heyderman, R. L. Stamps, *J. Phys. Condens. Matter* **25**, 363201 (2013).
13. I. Dzyaloshinsky, *J. Phys. Chem. Solids* **4**, 241–255 (1958).
14. T. Moriya, *Phys. Rev.* **120**, 91–98 (1960).
15. M. Bode *et al*., *Nature* **447**, 190–193 (2007).
16. S. Heinze *et al*., *Nat. Phys.* **7**, 713–718 (2011).
17. A. Fert, N. Reyren, V. Cros, *Nat. Rev. Mater.* **2**, 17031 (2017).
18. M. Heide, G. Bihlmayer, S. Blügel, *Phys. Rev. B* **78**, 140403 (2008).
19. J. P. Tetienne *et al*., *Nat. Commun.* **6**, 6733 (2015).
20. A. Thiaville, S. Rohart, E. Jue, V. Cros, A. Fert, *Europhys. Lett.* **100**, 57002 (2012).
21. S. Emori, U. Bauer, S. M. Ahn, E. Martinez, G. S. Beach, *Nat. Mater.* **12**, 611–616 (2013).
22. K. S. Ryu, L. Thomas, S. H. Yang, S. Parkin, *Nat. Nanotechnol.* **8**, 527–533 (2013).
23. F. Ummelen, H. Swagten, B. Koopmans, *Sci. Rep.* **7**, 833 (2017).
24. Materials and methods are available as supplementary materials.
25. M. Belmeguenai *et al*., *Phys. Rev. B* **91**, 180405 (2015).
26. H. Yang, A. Thiaville, S. Rohart, A. Fert, M. Chshiev, *Phys. Rev. Lett.* **115**, 267210 (2015).
27. S. Monso *et al*., *Appl. Phys. Lett.* **80**, 4157–4159 (2002).
28. I. M. Miron *et al*., *Nature* **476**, 189–193 (2011).
29. M. Baumgartner *et al*., *Nat. Nanotechnol.* **12**, 980–986 (2017).
30. L. Liu *et al*., *Science* **336**, 555–558 (2012).
31. K. Garello *et al*., *Nat. Nanotechnol.* **8**, 587–593 (2013).
32. G. Yu *et al*., *Nat. Nanotechnol.* **9**, 548–554 (2014).
33. S. Fukami, C. Zhang, S. DuttaGupta, A. Kurenkov, H. Ohno, *Nat. Mater.* **15**, 535–541 (2016).
34. Y. W. Oh *et al*., *Nat. Nanotechnol.* **11**, 878–884 (2016).
35. A. van den Brink *et al*., *Nat. Commun.* **7**, 10854 (2016).
36. K. Cai *et al*., *Nat. Mater.* **16**, 712–716 (2017).
37. S. Fukami, T. Anekawa, C. Zhang, H. Ohno, *Nat. Nanotechnol.* **11**, 621–625 (2016).
38. K. S. Lee, S. W. Lee, B. C. Min, K. J. Lee, *Appl. Phys. Lett.* **102**, 112410 (2013).
39. Z. Luo *et al*., Data from: Chirally coupled nanomagnets, Zenodo (2019).
40. A. Vansteenkiste *et al*., *AIP Adv.* **4**, 107133 (2014).

ACKNOWLEDGMENTS

We thank A. Weber, H. Arava, and V. Guzenko for technical support with sample fabrication. **Funding:** This work was supported by the Swiss National Science Foundation through grants 200021-153540, 200020-172775, and 200021-160186. J.C. has received funding from the European Union's Horizon 2020 research and innovation program under the Marie Skłodowska-Curie grant agreement 701647. Part of this work was carried out at the Surface/Interface: Microscopy beamline of the Swiss Light Source. **Author contributions:** This work is a partnership that was led jointly and equally by the L.J.H. and P.G. groups. Z.L., T.P.D., L.J.H., and P.G. conceived the work and designed the experiments; Z.L. fabricated the samples and performed the electrical measurements with the support of T.P.D. and E.K.; Z.L. analyzed and interpreted the data from the electrical measurements with the help of T.P.D. and P.G.; Z.L., J.V., A.K., T.P.D., J.C., M.B., T.S., and G.K. performed the X-PEEM measurements, which were interpreted by Z.L., J.V., and A.K.; A.H. performed the micromagnetic simulations; and Z.L., P.G., and L.J.H. worked on the manuscript together. All authors contributed to the discussion of the results and the manuscript revision. **Competing interests:** The authors declare no competing interests. **Data and materials availability:** All data used in this Report has been deposited in the Zenodo public database (*39*). The micromagnetic simulations were performed by using the open source code MuMax^3 (*40*).

SUPPLEMENTARY MATERIALS

www.sciencemag.org/content/363/6434/1435/suppl/DC1
Materials and Methods
Supplementary Text
Figs. S1 to S15
References (*41*, *42*)

17 July 2018; accepted 26 February 2019
10.1126/science.aau7913

Chirally coupled nanomagnets

Zhaochu Luo, Trong Phuong Dao, Aleš Hrabec, Jaianth Vijayakumar, Armin Kleibert, Manuel Baumgartner, Eugenie Kirk, Jizhai Cui, Tatiana Savchenko, Gunasheel Krishnaswamy, Laura J. Heyderman, and Pietro Gambardella

Science **363** (6434), . DOI: 10.1126/science.aau7913

Magnetic building blocks in two dimensions

Artificial magnetic structures can offer a variety of functionalities in spintronics devices. Luo *et al.* engineered magnetic domains in Pt/Co/AlO_X trilayers that had alternating in-plane and out-of-plane magnetizations. The regions interacted laterally through the so-called Dzyaloshinskii-Moriya interaction, which determined the relative sign and orientation of the magnetization in adjacent domains. Using the coupling between the domains, the researchers were able to engineer more-complex magnetic structures such as skyrmions and frustrated magnets.

Science, this issue p. 1435